

Cite this: *Nanoscale*, 2019, **11**, 16677

Catalytic manganese oxide nanostructures for the reverse water gas shift reaction†

Yulian He,^{a,b} Ke R. Yang,^{b,c} Ziwei Yu,^d Zachary S. Fishman,^{a,b} Laura A. Achola,^e Zachary M. Tobin,^e Jake A. Heinlein,^{a,b} Shu Hu,^{a,b} Steven L. Suib,^e Victor S. Batista^{*b,c} and Lisa D. Pfefferle^{*a}

Understanding the fundamental structure–property relationships of nanomaterials is critical for many catalytic applications as they comprise of the catalyst designing principles. Here, we develop efficient synthetic methods to prepare various MnO₂ structures and investigate their catalytic performance as applied to the reverse Water Gas Shift (rWGS) reaction. We show that the support-free MnO derived from MnO₂ 1D, 2D and 3D nanostructures are highly selective (100% CO₂ to CO), thermally stable catalysts (850 °C) and differently effective in the rWGS. Up to 50% conversion is observed, with a H₂/CO₂ feed-in ratio of 1:1. From both experiments and DFT calculations, we find the MnO₂ morphology plays a critical role in governing the catalytic behaviors since it affects the predominant facets exposed under reaction conditions as well as the intercalation of K⁺ as a structural building block, substantially affecting the gas–solid interactions. The relative adsorption energy of reactant (CO₂) and product (CO), $\Delta E = E_{\text{ads}}(\text{CO}_2) - E_{\text{ads}}(\text{CO})$, is found to correlate linearly with the catalytic activity, implying a structure–function relationship. The strong correlation found between $E_{\text{ads}}(\text{CO}_2) - E_{\text{ads}}(\text{CO})$, or more generally, $E_{\text{ads}}(\text{R}) - E_{\text{ads}}(\text{P})$, and catalytic activity makes ΔE a useful descriptor for characterization of efficient catalysts involving gas–solid interactions beyond the rWGS.

Received 2nd August 2019,
Accepted 13th August 2019

DOI: 10.1039/c9nr06078b

rsc.li/nanoscale

1. Introduction

Studies of fundamental relationships between structure and catalytic properties of materials are particularly valuable for the design and characterization of catalysts.^{1,2} In nanomaterials, the exposure of reactive surface planes is central for catalytic functionality and selectivity of specific reaction pathway.^{3,4} We focus on manganese oxides due to their high structural flexibility, variable valence and rich polymorphism. They are nontoxic, earth abundant and of great interests for a wide range of applications, including batteries, pseudocapacitors, and catalysis.^{5,6} In particular, MnO₂ is the most intriguing member of the family, with excellent performance in energy storage. So far, numerous reports have shown that many electrochemical properties of MnO₂ are highly dependent on morphological factors such as crystal structure, as well as size

and shape.^{4,7} In sharp contrast, their thermal catalytic properties have been investigated to a much lesser extent, despite that the reaction conditions are generally simpler with less interference from environmental factors than in electrochemistry.

Over the past few decades, the reverse Water Gas Shift (rWGS) reaction has been recognized as one of the most promising routes for effective CO₂ utilization. The reaction was brought to the forefront due to the added versatility of the products from the successive CO transformation.^{8–11} In industrial catalysis, the rWGS reaction is a key intermediate process for many other hydrogenation reactions, such as the Sabatier reaction,⁹ and methanol synthesis.¹⁰ To date, three types of heterogeneous catalysts have been primarily studied for the rWGS reaction, including metal catalysts such as Cu¹² and Pt;¹³ transition metal carbides (TMC) such as Mo₂C¹⁴ and TiC;¹⁵ and metal oxide catalysts such as Fe₃O₄⁸ and ZnO.¹⁶ While promising results have been reported, an outstanding challenge is the rational designs of catalysts with high efficiency, selectivity and thermal stability all together. Low operating temperatures (below 600 °C) have mostly been achieved by the addition of noble metals to facilitate reactant adsorption through their incompletely filled d-orbital electrons.¹⁵ The tradeoff, however, is poor selectivity, which in conjunction with the added costs of using precious metals renders this approach currently unfeasible.¹⁷ TMCs behave similarly to noble metals with lower cost but mostly suffer from poor selectivity with few

^aDepartment of Chemical and Environmental Engineering, Yale University, New Haven, CT 06520-8286, USA. E-mail: lisa.pfefferle@yale.edu

^bEnergy Sciences Institute, 810 West Campus Drive, Yale University, West Haven, CT, 06516, USA. E-mail: victor.batista@yale.edu

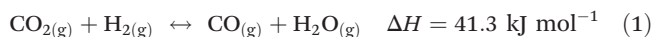
^cDepartment of Chemistry, Yale University, New Haven, CT 06520-8107, USA

^dCollege of Chemistry, Nankai University, Tianjin 300071, PR China

^eDepartment of Chemistry, University of Connecticut, Storrs, CT 06269-3060, USA

†Electronic supplementary information (ESI) available. See DOI: 10.1039/c9nr06078b

exceptions such as Mo_2C ,¹⁸ variables such as metal/carbon ratios can easily alter the surface chemistry under reaction conditions.¹⁵ Metal oxides are known to be highly selective but exhibit low conversion due to the loss of active sites in the reductive environment at high temperatures (above 600 °C),^{19,20} while higher temperatures are motivated in favour of the reaction thermodynamics (eqn (1)). So far, however, very few catalysts have achieved half conversion (50%) with a H_2/CO_2 feed-in ratio of 1 : 1 besides NiO supported on SBA-15 (55%) at 900 °C with 100% selectivity to CO and our own previous report on 1D hematite nanowires showing 55% conversion at 850 °C and 100% selectivity to CO,^{8,21,22} significant progress still needs to be accomplished in fundamental understanding of the reaction.



In this work, we introduce facile and highly efficient synthetic methods to prepare MnO_2 nanostructures with different nanodimensionality, including 1D α - MnO_2 nanowires, 2D (δ) - MnO_2 nanosheets and 3D ϵ - MnO_2 nanoflowers. We exploit a wide range of techniques, including SEM, (HR)TEM, AFM, XRD, XPS, physisorption, chemisorption and FTIR as well as DFT computational modeling to fully characterize the synthesized nanostructures. Remarkably, the three types of nanostructures exhibit different catalytic behaviors with respect to the rWGS reaction, while all of them show 100% selectivity and high thermal stability (850 °C). The systems are well characterized using a toolkit of experimental and theoretical techniques showing that the type of MnO_2 nanostructure is critical in governing its catalytic performance. A “Sabatier principle” type of analysis is performed to rationalize our experimental observations, through which we find the relative adsorption energy of reactant and product, $\Delta E = E_{\text{ads}}(\text{CO}_2) - E_{\text{ads}}(\text{CO})$, which can be modulated by the presence of K^+ ions, is linearly correlated with catalytic activity. This relative adsorption energy parameter ΔE is expected to be a useful descriptor for developing efficient catalysts for a wide range of heterogeneous catalytic reactions ruled by gas-solid interactions. In fact, ΔE should be a much more suitable descriptor than just the reactant adsorption energy itself, which has been extensively used in conjunction with Sabatier’s principle for constructing volcano plots of catalytic activity.²³ To the best of our knowledge, this paper represents the first study of the catalytic properties of MnO_2 nanomaterials towards the rWGS reaction.

2. Experimental section

All chemicals used here were purchased from Sigma-Aldrich with purity $\geq 97\%$. Ultrahigh purity (UHP) grade gases were purchased from Airgas.

2.1 Synthesis of α - MnO_2 nanowires

First, 160 mg of manganese(II) sulfate monohydrate $[\text{MnSO}_4 \cdot \text{H}_2\text{O}]$ was dissolved in 50 mL of hydrochloric acid

(pH = 1) and heated to the boiling point. Then 100 mg of potassium permanganate $[\text{KMnO}_4]$ was dissolved in 50 mL of hydrochloric acid (pH = 1) and added into the solution under magnetic stirring. The color of the solution changed from dark purple to dark brown immediately when the reactants were mixed. The solution was kept at boiling point and allowed to react for 3 hours under reflux conditions. The precipitate was then filtered and washed with excess deionized water to remove unreacted precursor ions. The remaining blackish powder sample was then vacuum dried overnight and crushed using mortar and pestle before further characterization and treatment.

2.2 Synthesis of (δ) - MnO_2 nanosheets

Manganese dioxide nanosheets were synthesized using a solution-based, template-free and low-temperature protocol. In a typical synthesis, 160 mg of manganese(II) sulfate monohydrate $[\text{MnSO}_4 \cdot \text{H}_2\text{O}]$ was dissolved in 50 mL of deionized water and heated to 80 °C. 100 mg of potassium permanganate $[\text{KMnO}_4]$ was dissolved in 50 mL of deionized water and then poured into the mixture under magnetic stirring. The color of the solution changed to dark brown immediately when the reactants were mixed, and was subsequently allowed to react for 2 hours at 80 °C. The precipitate was then filtered and washed with excess deionized water to remove unreacted precursor ions. The remaining brownish sample was then vacuum dried overnight and crushed using mortar and pestle before further characterization and treatment.

2.3 Synthesis of ϵ - MnO_2 nanoflowers

First, 160 mg of manganese(II) sulfate monohydrate $[\text{MnSO}_4 \cdot \text{H}_2\text{O}]$ was dissolved in 50 mL of hydrochloric acid (pH = 1) and heated to the boiling temperature. Then 100 mg of potassium permanganate $[\text{KMnO}_4]$ was dissolved in 50 mL of hydrochloric acid (pH = 1) and added dropwise in 30 minutes. The colour of the solution turned brown and got darker as the solution of potassium permanganate was dripped in. The solution was allowed to react under magnetic stirring for 2 hours under reflux. The precipitate was then filtered and washed with excess deionized water to remove any unreacted precursor ions. The remaining black sample was then vacuum dried overnight and crushed using mortar and pestle before further characterization and treatment.

2.4 H_2 -Temperature programmed reduction (TPR) and reverse water gas shift (rWGS) reaction

H_2 -TPR and the rWGS were performed on powder samples using a flow reactor set up. Mass flow controllers and k -type thermocouples were used to control gas flow rates and temperature, respectively. For TPR, 20 mg of sample was loaded into a straight tube quartz reactor with a rough silica bed and controllably heated from 100–900 °C at 10 °C min^{-1} . Over this period, composited feed gases with 10% H_2 (WHSV = 30 000 $\text{mL g}^{-1} \text{h}^{-1}$) and 90% Ar were flowed over the sample at a total flow rate of 100 mL min^{-1} . The outlet gas composition was measured using an SRS RGA 100 Mass Spectrometer.

The rWGS reactions were performed in the same set up used for H₂-TPR. 30 mg of catalyst of each sample was loaded into a straight tube quartz reactor and heated from 100–900 °C. The gas flow rate was 100 mL min⁻¹ and the inlet feed composition was 20% H₂ (WHSV = 40 000 mL g⁻¹ h⁻¹), 20% CO₂ (WHSV = 40 000 mL g⁻¹ h⁻¹) and 60% Ar. To quantify CO₂ conversion, the outlet gas composition was compared to measurements of the pre-reaction steady state CO₂ mass spectrometer signal. Using the eqn (2) below, CO₂ conversion was calculated at every data point. Measurements were taken approximately every 3 seconds. No change in Argon signal was observed indicating that the partial pressure in the chamber remained constant. Specific site time yield (STY) was calculated according to eqn (3) below to scale the reaction rate per unit area.

$$\% \text{ CO}_2 \text{ conversion} = \left(1 - \frac{\text{Measured CO}_2 \text{ signal}}{\text{Pre-reaction CO}_2 \text{ signal}} \right) \times 100\% \quad (2)$$

$$\begin{aligned} \text{Specific STY (mol s}^{-1} \text{ m}^{-2}) \\ = \frac{\text{Mass flow rate} \times \text{Conversion} \times \text{Time Window}}{\text{Reactor volume}} \times \text{Surface Area} \times \text{Weight} \\ \text{Volumetric Flow rate} \end{aligned} \quad (3)$$

2.5 Modeling

All Density Functional Theory (DFT) calculations were performed with the Vienna *Ab initio* Simulation Package (VASP)^{24–27} version 5.4. The visualization of structures was performed with the VESTA software package version 3.²⁸ We used the Perdew–Burke–Ernzerhof (PBE) exchange–correlation functional²⁹ in conjugation with the projected augmented-wave (PAW) method^{30,31} to describe the electron-ion interactions. The cutoff energy of the plane wave basis was chosen to be 450 eV. A Gaussian smear was used with a $\sigma = 0.1$ eV. The energy convergence criterion was set to be 10⁻⁴ eV per unit cell. To describe the highly correlated 3d electrons in Mn ions, we used the empirical+*U* correction implemented in VASP following Dudarev's approach³² to add on-site potentials to the d electrons of Mn to properly describe the electronic states. A value of 5 eV was used for the $U_{\text{eff}} = U - J$ parameter according to a DFT+*U* study by Wdowik and Legut.³³ Dispersion interactions were considered with Grimme's DFT-D3 method with Becke-Jonson damping.^{34,35}

MnO is an antiferromagnetic system with a type-II ordering (AFII). The ordering of magnetic moments of Mn²⁺ are parallel within the (111) planes, and anti-parallel between the adjacent layers (Fig. S16†).³³ In the paramagnetic phase, MnO has a rocksalt structure (space group *Fm* $\bar{3}$ *m*) with a lattice constant of 4.446 Å.³⁶ However, the lattice constant of the magnetic cell doubles when spins are taken into account for the anti-ferromagnetic state. We applied spin-polarized calculations to model the anti-ferromagnetic state of MnO. We used a 3 × 3 × 3 Monkhorst-Pack type *k*-point mesh³⁷ to sample the Brillouin zone during the geometry optimization of bulk MnO. The geometry convergence criterion was set to be energy

change of less than 10⁻³ eV per unit cell between two consequent steps.

We built slab models for MnO (200) and Mn (220) facets, including 6 layers of Mn–O units for both the MnO (200) and (220) slab models. Supercells with dimensions of 27.92 Å × 8.96 Å × 8.96 Å and 12.74 Å × 25.60 Å × 8.96 Å were used to model the MnO (200) and (220) surfaces. Monkhorst-Pack *k*-point meshes of 1 × 3 × 3 and 3 × 1 × 3 were used in the calculations of slab models of MnO (200) and (220), respectively. For K⁺-doped MnO, one of the surface Mn²⁺ ions was replaced by K⁺ and one of its nearby O²⁻ was replaced by OH⁻ to maintain the charge neutrality. The bottom three layers of atoms were frozen at their bulk positions, while the top three layers of atoms, as well as the adsorbed molecules were allowed to relax during geometry optimizations. The calculations of isolated H₂, CO₂, and CO molecules were performed using large supercells of 15 Å × 15 Å × 15 Å and a 1 × 1 × 1 Monkhorst-Pack *k*-point mesh. In the geometry optimization of slabs and molecules, the force convergence criterion was set to be 0.03 eV Å⁻¹. The adsorption energies were calculated according to eqn (4):

$$E_{\text{ads}} = E_{\text{slab+adsorbate}} - E_{\text{slab}} - E_{\text{adsorbate}} \quad (4)$$

where E_{slab} is the energy of a bare MnO slab, $E_{\text{adsorbate}}$ is the energy of an isolated adsorbate molecule, and $E_{\text{slab+adsorbate}}$ is the energy of a molecule adsorbed on a MnO slab. With this definition, a more negative E_{ads} corresponds to a stronger interaction between the surface and the adsorbed molecule.

2.6 Characterizations

More details on computations, coordinates of optimized structures, experiments and characterizations are available in the ESI.†

3. Results and discussion

3.1 Structures and compositions

The MnO₂ nanostructures were synthesized through our self-developed facile wet-chemical routes as discussed in the method section. The crystal structures of MnO₂ are largely diversified depending on how the basic structural unit [MnO₆] octahedrons are linked. There are three major categories of MnO₂ with different dimensionalities, including chain-like tunnel 1D structure α , β and γ ; sheet or layered 2D structure δ ; and 3D structure ϵ and λ . SEM and TEM images showed that our synthesized manganese oxide nanomaterials exhibit morphologies of nanowires, nanosheets and nanoflowers (Fig. 1). The nanowires (Fig. 1a & d) are 30–40 nm in thickness and 1–2 μ m in length while the nanoflowers (Fig. 1c & f) are approximately 500 nm in diameter. Those dimensions were also confirmed by Atomic Force Microscopy (Fig. S1†). The nanosheets greatly resemble graphene-like structures with wrinkled fringes, the thickness of which was found to be 2 nm through AFM (Fig. S1†).

The crystallinities and chemical compositions of nanowires, nanosheets and nanoflowers were found to be α -MnO₂ (PDF

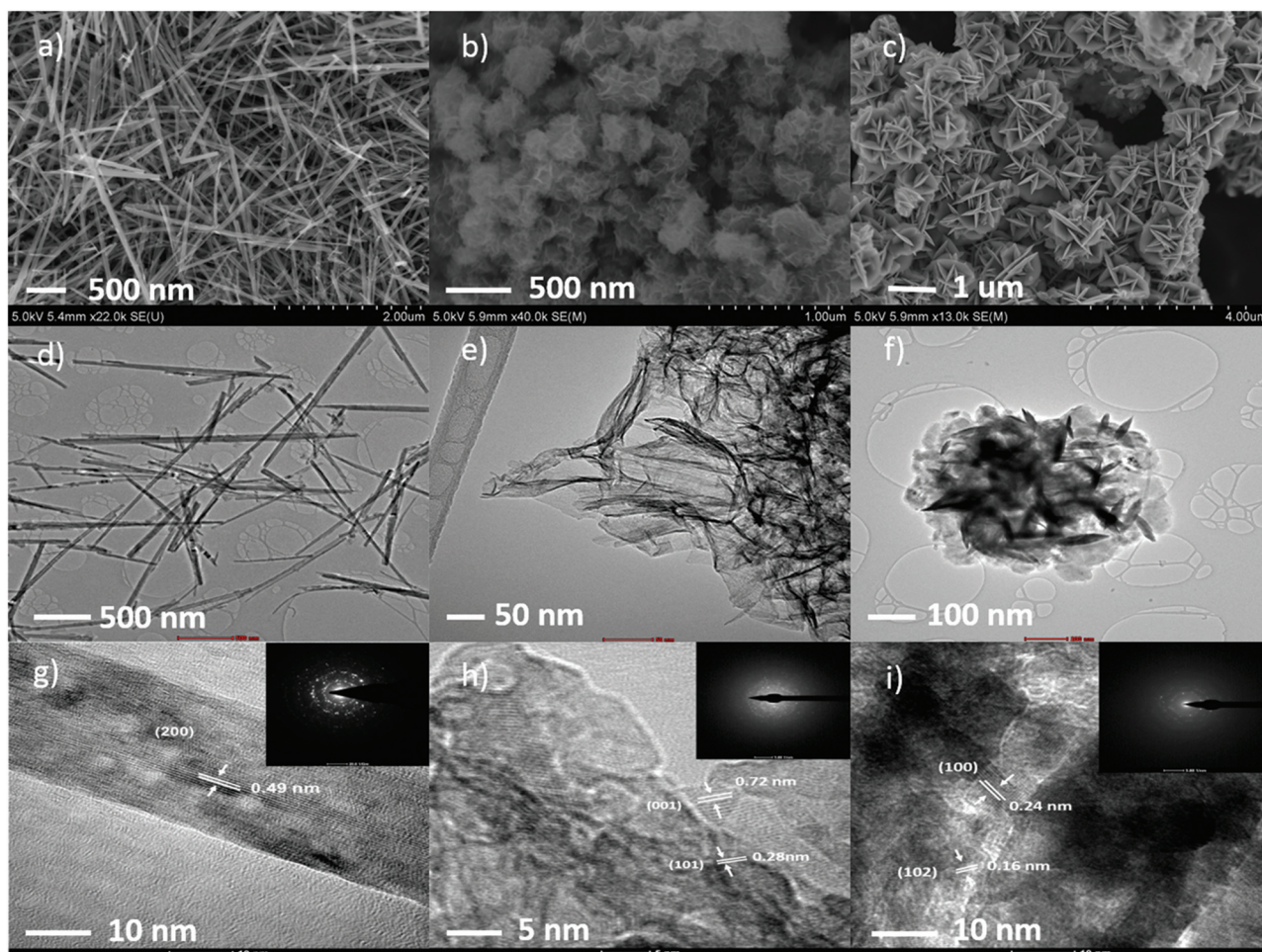


Fig. 1 SEM, TEM images of (a), (d) nanowires; (b), (e) nanosheets; (c), (f) nanoflowers. (g) High-resolution TEM image of α - MnO_2 nanowire together with the SAED pattern taken at the same location showing a basal spacing of 0.49 nm corresponding to the characteristic plane (200) of α - MnO_2 . (h) HRTEM image of MnO_2 nanosheets showing the polycrystallinity with various lattice spacings, primarily 0.72 nm corresponding to the characteristic (001) from δ polymorph; (i) HRTEM image of ϵ - MnO_2 nanoflowers showing basal spacings of 0.24 nm and 0.16 nm, corresponding to (100) and (102) planes, respectively.

No.: 01-072-1982), amorphous MnO_2 and ϵ - MnO_2 (PDF No.: 9014106), respectively, as confirmed by X-ray diffraction (Fig. S2†). Peak broadening in the diffraction patterns of all samples is commonly observed for nanomaterials with small crystallite sizes, as explained by the Scherrer equation.³⁸ The XRD patterns of nanosheets are not well-defined, possibly due to the poor crystallinity and instrumental detection limits for small particles. While two featured broad diffraction peaks at 37° and 67° were observed, suggesting a low crystallinity resulting from the absence of a long range ordered $[\text{MnO}_6]$ octahedral unit.³⁹ HR-TEM and selected area electron diffraction (SAED) were used to further investigate the crystallinity of the nanosheets (Fig. 1h). Several crystal facets were found but mostly the characteristic (001) from δ - MnO_2 diffraction planes with a basal spacing of 0.72 nm,⁴⁰ suggesting that the nanosheets primarily consist of local δ -birnessite structures.

High-resolution TEM analysis was also performed on the nanowires and nanoflowers (Fig. 1g & i), through which we

have again confirmed that both structures are crystalline as shown in the SAED ring patterns. In the nanowires, the crystal growth was found to occur along the (200) plane with a basal spacing of 0.49 nm, characteristic of the α -phase of MnO_2 and is not found in other phases.⁴¹ In the nanoflowers, (100) and (102) crystal planes were found with basal spacings of 0.24 nm and 0.16 nm, respectively. We have also noticed an anomalous peak at $2\theta = 22.5^\circ$ in the nanoflower XRD diffraction pattern (Fig. S2†), which cannot be assigned to any crystal plane but could arise from the strong (110) superlattice reflection of ϵ - MnO_2 .⁴²

Differences in the crystallinity of these nanostructures result from the different synthetic conditions. The crystal structure of the α - MnO_2 consists of 2×2 tunnels formed by edge- and corner-sharing $[\text{MnO}_6]$ octahedra. During the crystal growth, large cations from the precursors such as K^+ can enter the tunnels, balance the charges and stabilize the structure.⁴³ As one of the most thermodynamically stable forms, α - MnO_2

nanowires have been obtained mainly through hydrothermal approaches,⁴³ where high temperature, high pressure and long reaction time are always required. While in our nanowire growth, the energy inputs have been minimized as much as possible: the KMnO_4 solution was poured into MnSO_4 solution rapidly under an acidic environment upon refluxing for 3 hours. By precisely controlling the variables, we found the optimal precursor mass ratio, acidity, time, and temperature to initiate the nanowire growth. When any of the above-mentioned parameters is perturbed from the optimal values, the crystal growth either fails or proceeds accompanied by other side product formations, as shown in Fig. S3.†

By adding the KMnO_4 solution dropwise into MnSO_4 reaction vessel, instead of directly pouring as is the case for the nanowire synthesis, we were able to obtain the 3D flower-like $\epsilon\text{-MnO}_2$ nanostructure. $\epsilon\text{-MnO}_2$, also known as Akhtenskite, is composed of hexagonal unit cells with closely packed oxygen atoms and Mn^{4+} randomly occupying over 50% of the octahedral positions.⁴² Dropwise addition of KMnO_4 likely leads to different nucleation and crystallization rates and thus formation of different polymorphs by keeping a lower K^+ concentration at the nucleation sites when compared to the nanowire synthesis where many K^+ are needed for structure stabilization, even though both systems eventually reach at the same K^+ concentration. The densely packed arrangements of $\epsilon\text{-MnO}_2$ may have enabled itself to stabilize without the aid of any cation insertions. Indeed, as supported by our subsequent X-ray photoelectron spectroscopy analysis at K 2p and EDS mapping (Fig. 2c), we found no trace of K^+ in the nanoflower structure.

Both $\alpha\text{-MnO}_2$ nanowires and $\epsilon\text{-MnO}_2$ nanoflowers were synthesized under reflux with an acidic environment. The high temperature and high acidity have promoted the crystal construction into a more stable and compact structure to accommodate the harsh environment.⁴⁴ However, $(\delta)\text{-MnO}_2$ nanosheets were obtained under milder reaction conditions with lower temperature and neutral pH, which may account for its poor crystallinity (Fig. 1h).

To further characterize the surfaces and chemical compositions of these nanomaterials, X-ray photoelectron spectroscopy was performed as depicted in Fig. 2. All C 1s were fixed at 284.4 eV for spectra calibration (Fig. S4†). All samples were similar at Mn 2p (Fig. 2a), displaying the characteristic spin-orbit doublet of MnO_2 at 642.6 eV and 654.0 eV corresponding to Mn^{4+} 2p_{3/2} and Mn^{4+} 2p_{1/2}, respectively. An identifiable shape was also found for all samples at the top of Mn 2p_{3/2} peak, distinguishing MnO_2 from other manganese oxides. A detailed fitting analysis of the Mn 2p_{3/2} peak is shown in Fig. S5† using the models from Biesinger *et al.* with 6 peaks of equal FWHM,⁴⁵ all fitted spectra agree very well with a typical Mn 2p_{3/2} from MnO_2 standard. At O 1s (Fig. 2b), we found the characteristic binding energy peak for lattice oxygen located at 529.8 eV for all structures; however, 2D $(\delta)\text{-MnO}_2$ exhibited one additional peak at 533.5 eV that normally corresponds to surface hydroxyl groups. This observation is consistent with some previous reports that for layered $\delta\text{-birnessite MnO}_2$, a large number of water molecules or ions can exist in the interlayer regions.^{46,47} Our FTIR studies also yielded similar conclusions (Fig. S6†), suggesting the presence of hydroxyls in the nanosheets. Quantitative elemental analysis

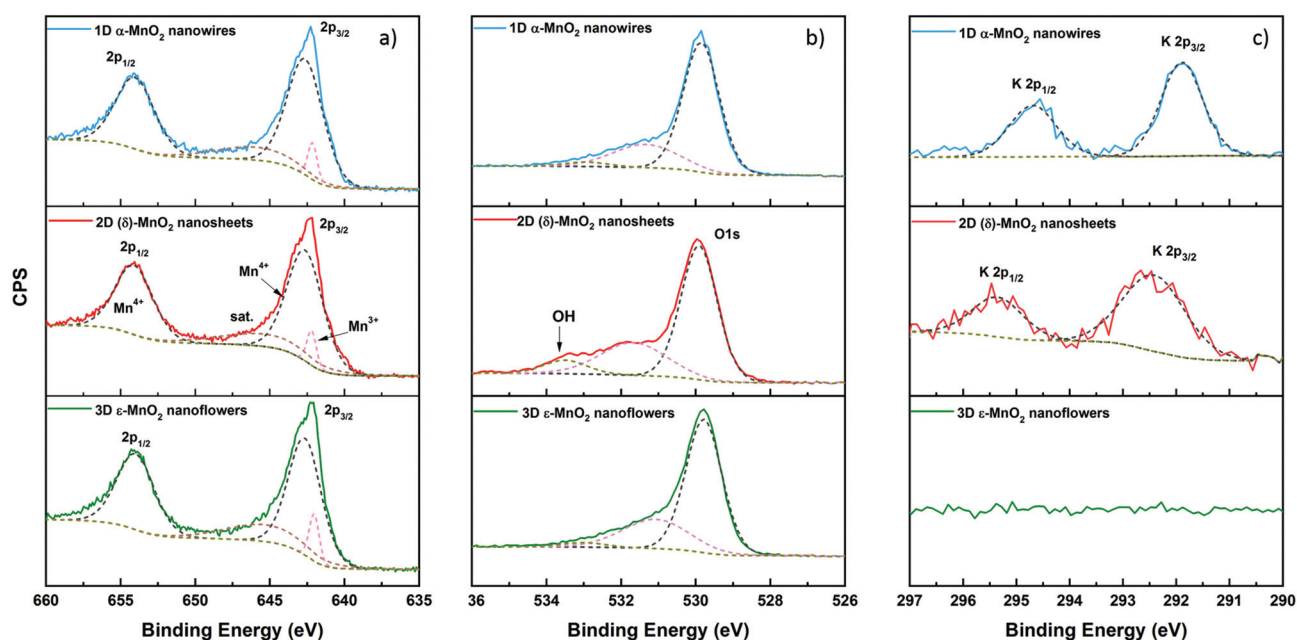


Fig. 2 XPS deconvolution spectra at (a) Mn 2p displaying Mn^{4+} 2p_{3/2} and 2p_{1/2} as well as the characteristic identifiable shape of MnO_2 ; (b) O 1s, from which we find that MnO_2 nanosheets possess hydroxyl groups in the structures; (c) K 2p, K^+ was found both in $\alpha\text{-MnO}_2$ nanowires and $(\delta)\text{-MnO}_2$ nanosheets but not in nanoflowers.

Table 1 Atomic concentrations from XPS, TPR and EDS

Samples	Mn ^a (%)	O ^a (%)	Mn : O ^a	K ^a (%)	K ^b (%)	Mn : O ^c
α-MnO ₂ nanowires	23.90	50.60	1 : 2.12	1.81	2.26	1 : 2.16
(δ)-MnO ₂ nanosheets	17.70	39.20	1 : 2.22	1.04	1.16	1 : 2.30
ε-MnO ₂ nanoflowers	25.30	51.40	1 : 2.03	0	0	1 : 2.04

^a From XPS. ^b From EDS elemental mapping analysis. ^c From TPR quantification.

can be conducted as suggested by eqn (S1),[†] Table 1a. We found the atomic ratio of Mn to O was about 1 : 2 for all samples with that of the nanosheets being the highest, presumably induced by the excessive hydroxyl species. This confirms once again that the chemical composition of our synthesized manganese oxide nanostructures is indeed MnO₂.

Significant differences were found at K 2p (Fig. 2c). First, no trace of K⁺ was seen in ε-MnO₂ nanoflowers, indicating that such densely packed structure is unable to accommodate large cations like K⁺ as we discussed previously, our EDS analysis on the nanoflowers also showed no trace of K⁺ (Table 1b). Second, quantitatively less K⁺ was found in the nanosheets than in the nanowires. Previous DFT studies suggest that placing K⁺ in the tunnels can stabilize α-MnO₂ due to the optimum K–O distance.⁴⁸ The calculated K⁺ binding energy indicates a strong interaction between K⁺ and the negative charged O atoms in the tunnels. Similarly, the layered MnO₂ can also accommodate K⁺ between the layers,⁴⁹ while the geometric arrangement of K⁺ and O atoms is not as good as that in α-MnO₂, resulting in a weaker K–O interaction and therefore less K⁺ observed. HAADF elemental mapping images were taken to give a more intuitive illustration of the distribution of K⁺ in the MnO₂ nanostructures in Fig. S7.[†]

3.2 Catalytic properties

3.2.1 Temperature-programmed reduction. To study the reducibility of the materials, we performed the temperature programmed reduction (TPR) on the three MnO₂ samples with 10% H₂ (WHSV = 30 000 mL g^{−1} h^{−1}) and 90% Ar for a total flow rate of 100 mL min^{−1} (Fig. 3). Significant differences were found among samples in their responses to H₂. Two similar H₂ consumption peaks were detected in all TPR reactions, indicating that the reduction of MnO₂ in H₂ is stepwise regardless of the nanodimensionality. XRD was used here to study the chemical transformations *ex situ* during the TPR processes, samples were recollected directly after each reduction peak and analyzed (Fig. S8[†]). Results suggest that MnO₂ was first reduced into Mn₃O₄ before further reduction to MnO, as illustrated by eqn (5) & (6). This is consistent with the reduction behaviors of manganese oxides reported in the literature.⁵⁰



While the TPR profile of 2D (δ)-MnO₂ nanosheets showed one more consumption peak at 100 °C in addition to the two reduction peaks, which is attributed to the dehydration of the

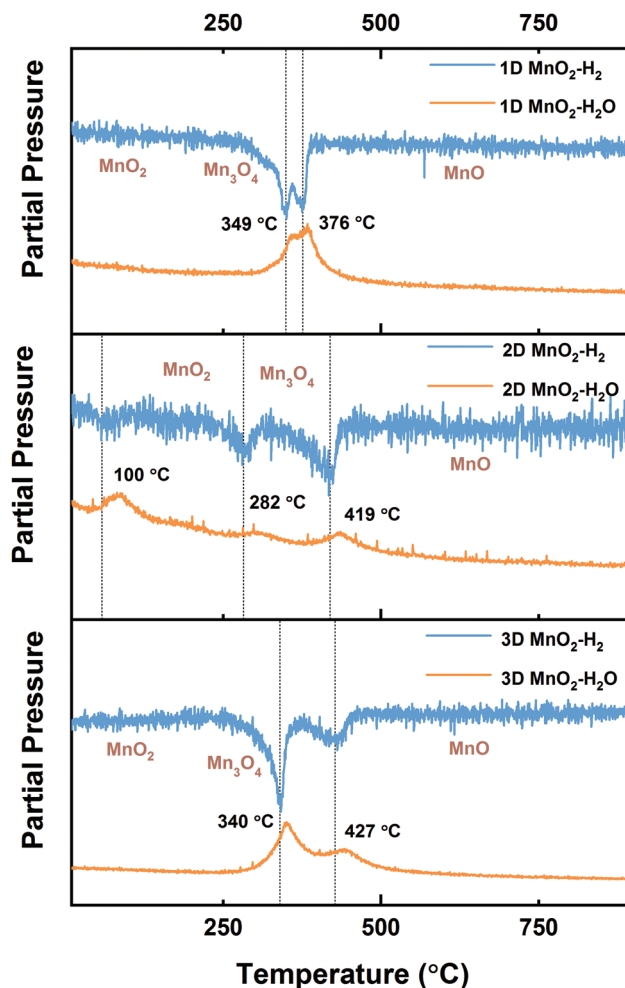


Fig. 3 H₂-Temperature programmed reduction profiles from top to bottom: nanowires, nanosheets and nanoflowers. All samples presented two (primary) H₂ consumption peaks indicating the stepwise reduction from (1) MnO₂ → Mn₃O₄, (2) Mn₃O₄ → MnO. MnO₂ nanosheets showed one more peak at 100 °C corresponding to dehydration.

hydroxyl groups present in the structure. XRD was taken before and after the dehydration and no changes were revealed (Fig. S8b[†]). A quantitative analysis was performed through peak area integration to quantify the stoichiometric ratios of Mn : O in the bulk as compared to that of the surface calculated from XPS, Table 1c. However, no significant difference was detected between the bulk and the surface ratios. Additionally, SEM images were taken here to study the morphological evolutions for all samples after H₂-TPR, the nano-

structures were found altered and became more crystalline as they were converted into MnO (Fig. S9†).

3.2.2 The reverse water gas shift reaction. The reverse water gas shift reaction was conducted using the same reactor setup as TPR with 20% H₂ (WHSV = 40 000 mL g⁻¹ h⁻¹), 20% CO₂ (WHSV = 40 000 mL g⁻¹ h⁻¹) and 60% Ar for a total flow rate of 100 mL min⁻¹. With the same mass loadings, the percentage CO₂ conversion calculated as described in eqn (2) is plotted against temperature in Fig. 4a together with the thermodynamic equilibrium with a 1:1 H₂/CO₂ feed-in ratio.⁵¹ All samples showed 100% CO selectivity with no other by-products (*e.g.* CH₄, CH₃OH) detected in the mass spectrometer across the entire reaction temperatures, complete mass spectra are shown in Fig. S10.† The complete selectivity to CO at lower temperatures (<700 °C) adds great value to the catalysts as the strong competition with CO₂ methanation side reaction can lead to a higher H₂ consumption thus lowering syngas production,⁵² while the methanation reaction is naturally suppressed due to the thermodynamic limitations at higher temperatures (>700 °C), which makes CO the governing product, resulting in high selectivity.²¹ The light-off temperatures for all MnO₂ nanostructures appeared to be very similar at around 450 °C, where the most thermodynamically stable form was

found to be MnO through our TPR studies, suggesting that the nanostructured MnO₂ were transformed into MnO before the onset of the rWGS. This is also supported by our *ex situ* XRD analysis (Fig. S11†), implying that the true active species for the reaction is MnO. While interestingly, simply starting with MnO structures (nano or bulk, with or without K⁺) instead of MnO₂ did not give any activity for this reaction (Fig. S12†), suggesting that the reduction from MnO₂ to MnO is essential to initiate the reaction.

Even though the true active species was found to be MnO in all cases and their crystal structures became similar after the transition (Fig. S11†), we found MnO₂ with different initial morphologies exhibited different reaction behaviors. At low temperatures (below 630 °C) and with the same mass loadings, 3D ε-MnO₂ nanoflowers exhibited the highest activity with CO₂ conversion up to 13% (Fig. 4a). However, as temperature increased, it became less effective: the CO₂ conversion decreased to 10% at 730 °C and then increased slightly to 20% at 900 °C. 2D (δ)-MnO₂ nanosheets showed the best activity at high temperatures, reaching a maximum of 50% CO₂ conversion at 850 °C approaching to equilibrium, while 1D α-MnO₂ nanowires showed a slightly lower maximum of CO₂ conversion of 43% at 890 °C. As a control, commercial MnO₂

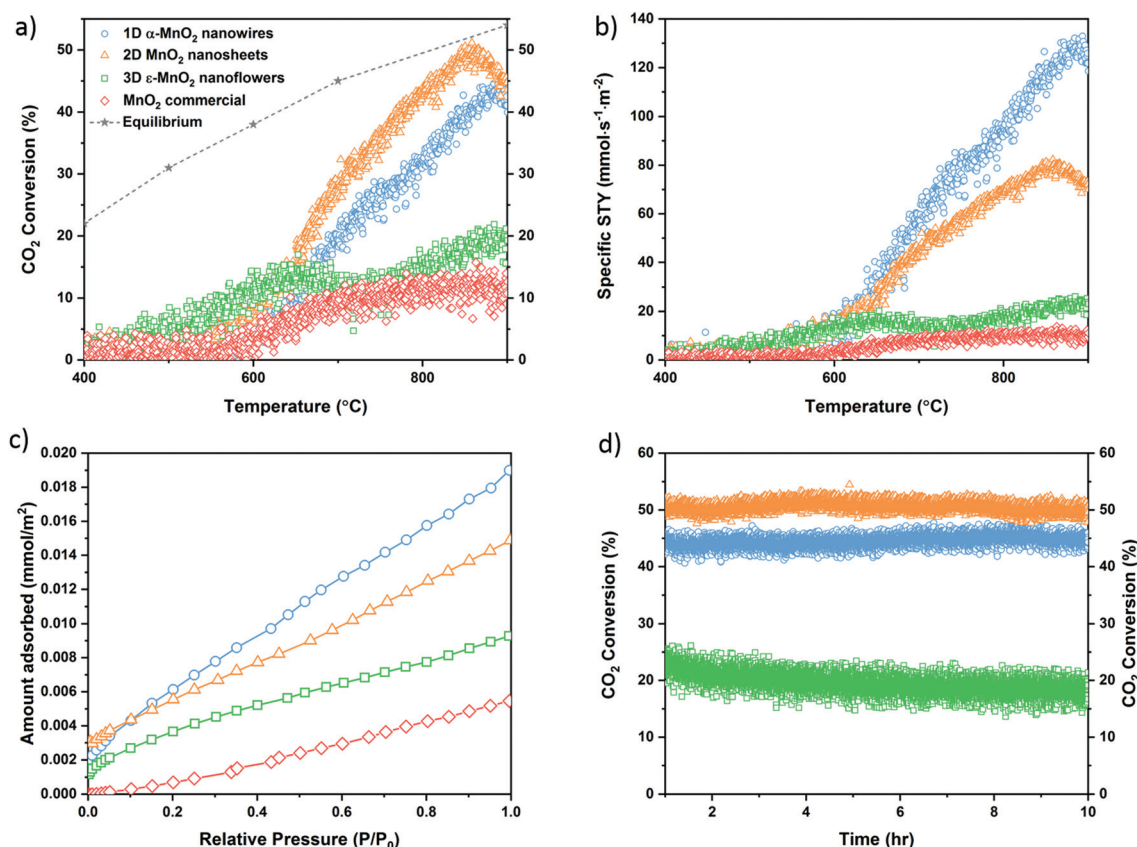


Fig. 4 (a) %CO₂ conversion plotted against temperature in rWGS upon the same catalyst mass loading of different structures together with thermodynamic equilibrium. (b) Specific site time yield (STY) plotted as a function of temperature in rWGS reaction. (c) CO₂ adsorption isotherms for all MnO samples on a per surface area basis at 298 K. (d) Stability tests over 10 hours at 850 °C exhibiting high thermal stability of all three structures. Stability tests at 600 °C can be found in Fig. S13.†

particles (no K^+) were tested under the same conditions to determine the effect of nanostructure. Unsurprisingly, all nanoscale MnO_2 outperformed commercial MnO_2 particles, the CO_2 conversion of which stayed below 12% at all times. To our knowledge, this is the first study on the catalytic activity of MnO_2 nanomaterials applied to the rWGS reaction.

To test the thermal stability of our MnO_2 catalysts, the reaction was kept at 850 °C (Fig. 4d) over 10 hours. Remarkably, all samples exhibited high thermal stability with negligible activity loss (Fig. 4d), which is rarely seen within metal oxide catalysts such as ZnO and Fe_2O_3 , especially in the absence of supports.²⁰ To ensure the measurements are taken under kinetic regime, additional stability tests were conducted at 600 °C where the CO_2 conversions are further away from equilibrium (Fig. S13†), again, all three structures exhibited high stability over 10 hours. Both 1D and 2D support-free MnO_2 nanostructures showed outstanding catalytic performance with almost 50% conversion, 100% selectivity to CO and high temperature stability, compared to other reported catalysts where the half conversion is rarely achieved.²¹ A comparative table including the reaction conditions and the catalytic performance of this work and some other reports can be found in the ESI, Table S1.†

XPS analysis at C 1s and thermogravimetric analysis were performed to study the carbon deposition on the catalysts after the reaction, Fig. S14a.† At XPS C 1s, carbonate species at 288.9 eV were detected for all three structures while to a different extent: 5.6%, 3.2% and 0.9% for MnO derived from nanowires, nanosheets and nanoflowers, respectively. This can be due to the adventitious carbon as well as the chemisorbed CO_2 on metal oxide surfaces and has been previously reported in TiO_2 ,⁵³ MgO ,⁵⁴ CaO ,⁵⁵ CuO ,⁵⁶ *etc.* The peak at 284.8 eV is ascribed to adventitious carbon, the atomic concentration of which is found to be 5.1%, 10.2% and 9.8% for 1D, 2D, and 3D MnO_2 derivatives, respectively. TGA analysis in air on the three structures showed negligible weight loss: 1.4%, 1.1% and 0.6% for 1D, 2D, and 3D structures, Fig. S14b–d,† which is likely due to the release of CO_2 from the surface carbonate

species and this trend matches well with the carbonate concentrations calculated from XPS analysis. Both evidences indicate a high resistance of these MnO_2 nanostructures to carbon deposition or “coking” under the reaction conditions.

The catalytic responses of 1D and 2D MnO_2 agree well with the fact that the rWGS is an endothermic process where high temperature favors the forward reaction. Both structures (1D & 2D) showing the trace of K^+ outperformed those without (3D & commercial) at high temperatures. To investigate the effect of K^+ promotion in this system, the nanosheets were sonicated in deionized water for 20 minutes and washed with excessive water to remove the residual K^+ . Note that the morphology of the nanosheets was not perturbed by sonication as confirmed by our microscopic studies (Fig. 1). Through XPS we found the K 2p intensity decreased after washes (Fig. S15a†). Interestingly, the catalytic activity also dropped as some K^+ was removed, with a maximum CO_2 conversion of 33%, but still higher than the unpromoted structures (nanoflowers & commercial, Fig. S15b†), suggesting that K^+ in the MnO_2 nanostructures does affect their catalytic performance.

Surface area measurements on the true catalyst MnO were performed to scale the catalytic performance per unit area by taking the sample out at 500 °C and converted to specific site time yield (STY), see Table S2† & Fig. 4b. Overall, all three nanostructured MnO_2 catalysts still outperformed the commercial, showing the merits of nanocatalysts compared to their bulk counterparts. Notably, distinctions still existed among different structures after normalization: the nanowires now exhibit a better catalytic performance over nanosheets followed by nanoflowers. A more detailed study on the catalyst structures under reaction conditions was conducted through HR-TEM (Fig. 5). The primary exposed facets were found different, with MnO (220) for nanowires, MnO (200) for nanosheets and MnO (220) & (200) for nanoflowers. This implies that although the three MnO_2 nanostructures have all been converted into MnO under reaction conditions with similar crystallinity as suggested by XRD (Fig. S11†), the initial morphology is still important as it affects the primary exposed

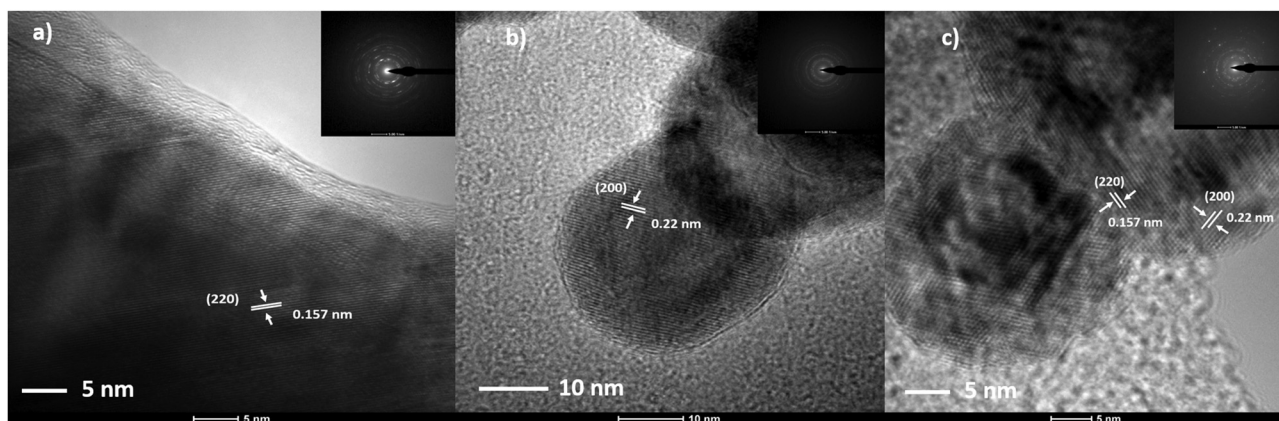


Fig. 5 HR-TEM studies on MnO derived from MnO_2 (a) nanowires, (b) nanosheets and (c) nanoflowers under reaction conditions. The primary exposed facets were found to be (220) for nanowires, (200) for nanosheets and (220) & (200) for nanoflowers.

facets during the structural evolution, which may substantially affect the catalytic performance. As later suggested by our CO₂ chemisorption studies (Fig. 4c), we found MnO evolved from 1D structure adsorbed the most CO₂ followed by that from 2D, 3D, and then commercial, which agrees perfectly with our experimental observations on their respective catalytic activities as well as the carbonate concentration calculated from XPS analysis. These results suggest that the difference in catalytic performance of these MnO structures is correlated to their distinct interactions with CO and CO₂, as determined by the underlying catalyst structures. Insights at the molecular level are provided by the DFT analysis.

3.3 DFT calculations

All computational details can be found in the method section. Taken from HRTEM (Fig. 5), we first built models for the two observed primary exposed facets: MnO (200) and MnO (220). On the MnO (200) surfaces, there are five-coordinate Mn and O sites, Mn_{5c} and O_{5c}, while on MnO (220), the surface Mn and O atoms are 4-coordinate, denoted as Mn_{4c} and O_{4c} (Fig. S17†). Here we considered the adsorption of CO₂, H₂, and CO on both surfaces (Fig. 6). On MnO (200), CO₂ is chemically

adsorbed at the O_{5c} position with a calculated adsorption energy of -0.76 eV. The adsorbed CO₂ resembles a carbonate-like structure with a C–O_{5c} bond length of 1.43 Å and two C–O bond lengths of 1.26 Å (Fig. 6a). Two O atoms from the adsorbed CO₂ molecule interact with two nearby Mn_{5c} atoms, featuring an O–Mn_{5c} distance of 2.27 Å. While on MnO (220), which is unsaturated in coordination, the adsorption energy of CO₂, -2.52 eV, is much more negative, meaning it's more strongly bound to the surface O_{4c} atom with a shorter C–O_{4c} bond (1.35 Å) and two C–O bonds of 1.28 Å (Fig. 6b). The carbonate-like structures of adsorbed CO₂ on MnO (200) and (220) surfaces are consistent with previous studies of CO₂ adsorption on metal oxide surfaces as discussed above in Fig. S14.† The structures of chemically adsorbed CO molecules on MnO (200) and (220) surfaces resemble the structure of a Mn–COO[−] carboxyl group (Fig. 6) with a C=O bond length of 1.22 Å, a C–O_{5c} of 1.51 Å and a C–Mn_{5c} of 2.22 Å on MnO (200), while the same C=O bond length of 1.22 Å, a C–O_{4c} of 1.40 Å, and a C–Mn_{4c} of 2.20 Å on MnO (220). The shorter C–O bond length as well as the more negative adsorption energy together imply a stronger interaction between CO and MnO (220). Additionally, the adsorption energies of CO on both surfaces

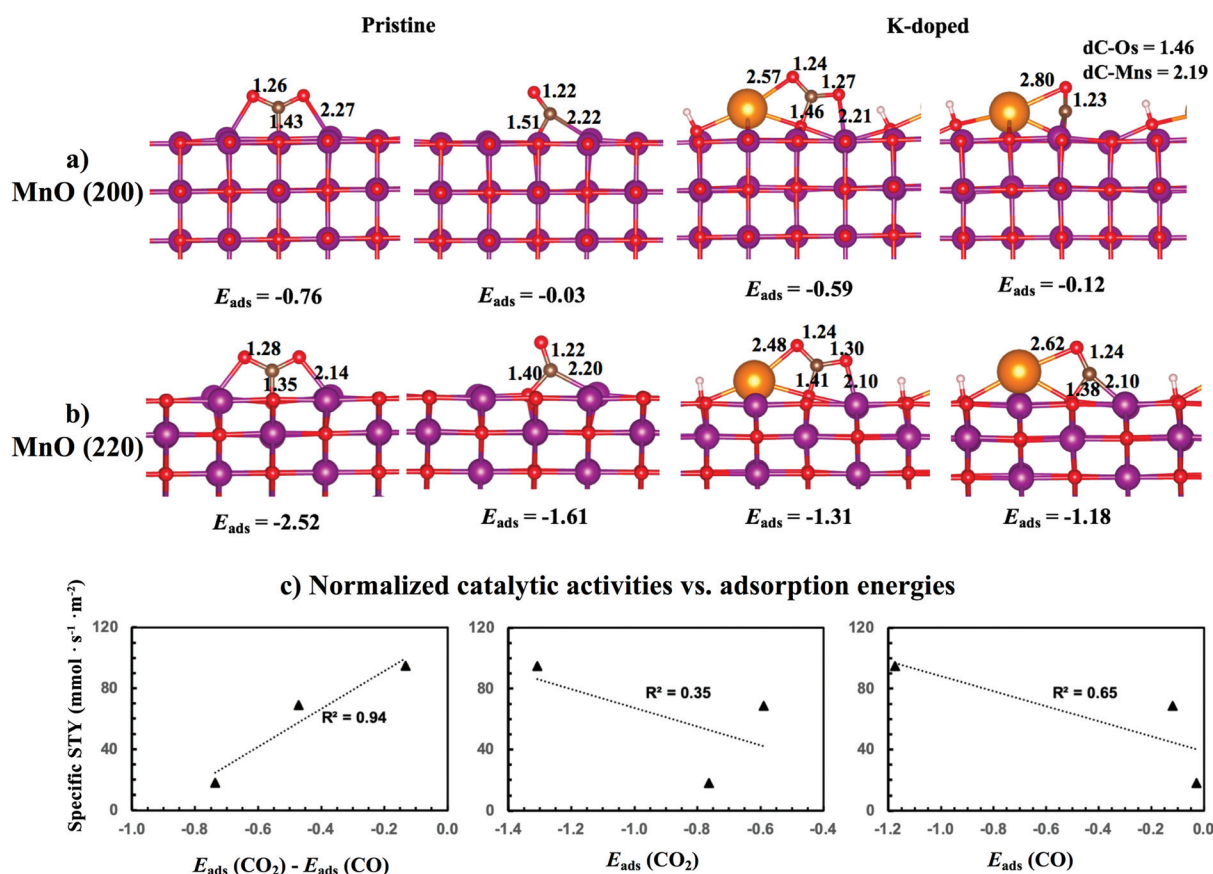


Fig. 6 Optimized structures and corresponding adsorption energies of CO₂ and CO on pristine and K⁺-doped (a) MnO (200) and (b) (220) surfaces. (c) Correlations between the measured specific STY at 800 °C and the calculated adsorption energies of CO₂ and CO and their differences. Purple, brown, red, orange, and white balls represent Mn, C, O, K, and H atoms, respectively. Key bond lengths are shown in the unit of Å and the calculated adsorption energies are in the unit of eV.

are much less negative than those of CO₂. In other words, the reduced CO product is unable to compete with CO₂ in binding to MnO surfaces for further reduction, which may account for the observed high selectivity toward CO.

The calculated adsorption energy of H to MnO (200) is 0.92 eV (Fig. S18†), suggesting its preference to stay as H₂ in the gas phase rather than be dissociatively adsorbed. On MnO (220), however, the H adsorption energy is −0.46 eV due to the unsaturation of O atoms. While favorable, it is still less negative than that of CO₂ and CO, suggesting that the dissociative adsorption of H₂ is less favorable than either the reactant CO₂ or the product CO. These findings imply that CO₂ reduction on MnO surfaces may proceed through a mechanism in which CO₂ binds to MnO surfaces first followed by H₂ reduction of the surface-bound CO₂ to surface-bound CO, completed by release of the CO product and formation of a new surface-bound CO₂.

We now turn our attention to investigate the effect of K⁺ promotion on the adsorption energies and its implications on the catalytic performance. We constructed K⁺-doped MnO (200) and (220) surfaces by replacing a surface Mn²⁺ by K⁺ and its neighboring O^{2−} by OH[−]. Upon geometric relaxation, K⁺ are found on top of the surfaces due to the large ionic radius (Fig. S17†). The optimized structure of chemically adsorbed CO₂, CO and H on both surfaces along with associated adsorption energies are shown in Fig. 6a and b and Fig. S17.† Doping MnO (200) with K⁺ slightly alters the adsorption energies of gas molecules (within 0.2 eV), while on MnO (220), significant positive shifts are observed for all gas adsorption energies. These results suggest that K⁺ doping can greatly affect the activity of MnO surfaces by modulating the gas adsorption energies, which is in line with studies of alkaline promotion effects for both forward⁵⁷ and reverse water gas shift reaction⁵⁸ in supported Pt/metal oxide systems.

Now we address structure–property relationships. According to the Sabatier principle, interactions between catalysts and reactants (or products) should be “just right” for optimal catalytic activity. If the interaction is too weak, the species may fail to bind, while if it is too strong, the adsorbed species may fail to desorb thus poisoning the catalyst.⁵⁹ Graphically, a volcano curve should be obtained when plotting the catalytic activity such as turnover frequency (TOF) against the adsorption energy of the key surface species.⁶⁰ Here we apply the similar analysis to rationalize our experimentally observed catalytic activities of the different MnO catalysts. As suggested by XPS (Fig. S19†), MnO derived from both nanowire and nanosheet still contain K⁺ in the structures. Therefore, we consider K–MnO (220), K–MnO (200), MnO (200) & (220) as suitable theoretical models for 1D, 2D and 3D structures, respectively. Here we use the specific STY (Fig. 4b) at 800 °C to represent the catalytic activities of different MnO catalysts. When plotting the specific STY against adsorption energies of CO₂ and CO (denoted as $E_{\text{ads}}(\text{CO}_2)$ and $E_{\text{ads}}(\text{CO})$) for different structures (Fig. 6c), we find no obvious correlation between the CO₂ adsorption energy and catalytic activity, while the catalyst with a more negative/favorable $E_{\text{ads}}(\text{CO})$ seems to have a greater

activity, contradictory to the Sabatier principle. However interestingly, the adsorption energy difference between CO₂ and CO correlates very well with the specific STY with a R^2 value of 0.94. These correlations between the gas adsorption energies and catalytic activities as well as the linear dependence were also observed at various temperatures, Fig. S20,† which implies that the key to the good catalytic performance in this system may not rely solely on either reactant adsorption or product desorption processes, but more on the adsorption–desorption balance on the MnO surfaces.

Taking both our experimental results and computational analysis into account, we propose that the difference in how these MnO catalysts perform under rWGS reaction conditions is related to both the primary exposed facets and the effect of K⁺ promotion, which is essentially governed by the morphology of the initial MnO₂. 1D α -MnO₂ nanowires, giving the highest experimental specific activity, are found to possess the best adsorption–desorption balance due to the high surface-coordination unsaturation on MnO (220) as well as K⁺ promotion through DFT. For 2D (δ)-MnO₂ nanosheets, the primary exposed facet was found to be MnO (200), which is less reactive toward gas phase adsorptions when compared to MnO (220), but the modulations of adsorption energies caused by K⁺ still improve the adsorption–desorption balance, giving the second highest experimental specific activity. With the co-existence of MnO (200) & (220) but the lack of K⁺ promotion, the 3D ϵ -MnO₂ nanoflowers showed the lowest specific activity at high temperatures. Additionally, the greater performance of 3D structure over others at low temperature regime may be due to the initial strong interaction between CO₂ and MnO (220). While when temperature increased, the strong CO adsorption on MnO (220) can poison the surface, thus resulting in a dip in the catalytic activity as observed experimentally. The subsequent slight increase might benefit from the reaction taking place on MnO (200), which is found to possess a better adsorption–desorption balance.

We also notice that the high selectivity of our MnO catalysts coincides with the fact that $E_{\text{ads}}(\text{CO}_2)$ is more negative/favorable than $E_{\text{ads}}(\text{CO})$ under all circumstances. A stronger interaction between the catalyst and reactant over product is the key to high selectivity as the product side reactions can be suppressed due to the less favorable adsorptions. Supported metal catalysts such as Cu¹² and Pt¹³ suffering from poor selectivity toward CO product are known to bind CO strongly. Based on this observation, we conclude that the catalyst with a positive $\Delta E = E_{\text{ads}}(\text{CO}_2) - E_{\text{ads}}(\text{CO})$, namely, $E_{\text{ads}}(\text{CO}_2)$ less negative/favorable, has a lower selectivity for rWGS. Thus, $\Delta E = E_{\text{ads}}(\text{CO}_2) - E_{\text{ads}}(\text{CO})$, or more generally, $\Delta E = E_{\text{ads}}(\text{R}) - E_{\text{ads}}(\text{P})$, may be a useful descriptor for developing more efficient and selective catalysts.

4. Conclusions

In this work, we have introduced simple synthetic routes to obtain MnO₂ nanostructures with different dimensionalities

including 1D α -MnO₂ nanowires, 2D (δ)-MnO₂ nanosheets and 3D ϵ -MnO₂ nanoflowers. We found that the resulting nanostructures were thermally stable (850 °C) and catalytically active towards CO₂ to CO conversion. The conversion efficiency is as high as 50% in the reverse Water Gas Shift reaction (rWGS), with 100% selectivity. We used an assortment of characterization tools including SEM, (HR)TEM, AFM, XRD, XPS, BET, and FTIR as well as DFT computational modeling to fully characterize the three systems. Under rWGS reaction conditions, the transition from MnO₂ to MnO was shown to be essential for the reaction initiation. Moreover, the initial morphology of MnO₂ played a significant role on the catalytic performance as it affects both the primary exposed facets after the structural evolution as well as the amount of K⁺ intercalation from the synthesis. Based on DFT modeling, we found that the adsorption energies of CO₂, CO and H₂ vary significantly with different exposed facets and can be tuned through K⁺ doping. Finally, we proposed that the catalytic performance of these MnO catalysts does not rely solely on either the reactant adsorption or product desorption processes, but on the adsorption–desorption energy difference of CO₂ and CO: $\Delta E = E_{\text{ads}}(\text{CO}_2) - E_{\text{ads}}(\text{CO})$. In fact, ΔE might be a more suitable descriptor than just the reactant adsorption energy itself that has been extensively used in conjunction with Sabatier's principle for constructing volcano plots of catalytic activity. The strong correlation between $E_{\text{ads}}(\text{CO}_2) - E_{\text{ads}}(\text{CO})$, or more generally, $E_{\text{ads}}(\text{R}) - E_{\text{ads}}(\text{P})$, and catalytic activity suggests that the binding energy difference between reactants and products should be a useful descriptor of efficient and selective catalysts for a wide range of heterogeneous processes involving gas–solid interactions, beyond the rWGS reaction.

Author contributions

Y. H. and L. D. P. designed the experiments and wrote the manuscript. K. R. Y. and V. S. B. conducted the DFT calculations and wrote the computation section. Y. H., Z. Y. and J. A. H. performed the experiments and characterizations. Z. S. F. and S. H. conducted physisorption. L. A., Z. M. T. and S. L. S. helped with chemisorption and manuscript improvement.

Conflicts of interest

There are no conflicts to declare.

Acknowledgements

Y. H. and L. D. P. would like to graciously thank Army Research Laboratory for generous support of funding for this research under ARO grant #64935, Agreement W911NF1410564, and thank the YINQE facilities and Dr Michael Rooks for providing access to and assistance with TEM, SEM, and AFM instruments. V. S. B. and K. R. Y.,

acknowledges an allocation of high-performance computer time from the National Energy Research Scientific Computing Center (NERSC) and support by the Air Force Office of Scientific Research (AFOSR) grant #FA9550-13-1-0020. The project made use of the Chemical and Biophysical Instrumentation Center at Yale University. The XPS work was performed under the instruction of Dr Min Li using PHI VersaProbe II X-ray Photoelectron Spectrometer at Yale West Campus Materials Characterization Core.

References

- 1 K. Qian, Z. Qian, Q. Hua, Z. Jiang and W. Huang, *Appl. Surf. Sci.*, 2013, **273**, 357–363.
- 2 K. Kalantar-zadeh, J. Z. Ou, T. Daeneke, A. Mitchell, T. Sasaki and M. S. Fuhrer, *Appl. Mater. Today*, 2016, **5**, 73–89.
- 3 J. Pal, C. Mondal, A. K. Sasmal, M. Ganguly, Y. Negishi and T. Pal, *ACS Appl. Mater. Interfaces*, 2014, **6**, 9173–9184.
- 4 M. Huang, F. Li, F. Dong, Y. X. Zhang and L. L. Zhang, *J. Mater. Chem. A*, 2015, **3**, 21380–21423.
- 5 S. Deng, L. Wang, T. Hou and Y. Li, *J. Phys. Chem. C*, 2015, **119**, 28783–28788.
- 6 V. Subramanian, H. Zhu, R. Vajtai, P. Ajayan and B. Wei, *J. Phys. Chem. B*, 2005, **109**, 20207–20214.
- 7 F. Cheng, Y. Su, J. Liang, Z. Tao and J. Chen, *Chem. Mater.*, 2010, **22**, 898–905.
- 8 Z. S. Fishman, Y. He, K. R. Yang, A. W. Lounsbury, J. Zhu, T. M. Tran, J. B. Zimmerman, V. S. Batista and L. D. Pfefferle, *Nanoscale*, 2017, **9**, 12984–12995.
- 9 H. Wu, Y. Chang, J. Wu, J. Lin, I. Lin and C. Chen, *Catal. Sci. Technol.*, 2015, **5**, 4154–4163.
- 10 J. Xu, X. Su, X. Liu, X. Pan, G. Pei, Y. Huang, X. Wang, T. Zhang and H. Geng, *Appl. Catal., A*, 2016, **514**, 51–59.
- 11 E. Ruckenstein and Y. H. Hu, *J. Catal.*, 1996, **162**, 230–238.
- 12 C.-S. Chen, W.-H. Cheng and S.-S. Lin, *Appl. Catal., A*, 2003, **238**, 55–67.
- 13 A. Goguet, F. C. Meunier, D. Tibiletti, J. P. Breen and R. Burch, *J. Phys. Chem. B*, 2004, **108**, 20240–20246.
- 14 X. Zhang, X. Zhu, L. Lin, S. Yao, M. Zhang, X. Liu, X. Wang, Y.-W. Li, C. Shi and D. Ma, *ACS Catal.*, 2016, **7**, 912–918.
- 15 J. A. Rodriguez, J. Evans, L. Feria, A. B. Vidal, P. Liu, K. Nakamura and F. Illas, *J. Catal.*, 2013, **307**, 162–169.
- 16 T. Shido and Y. Iwasawa, *J. Catal.*, 1993, **140**, 575–584.
- 17 K. Oshima, T. Shinagawa, Y. Nogami, R. Manabe, S. Ogo and Y. Sekine, *Catal. Today*, 2014, **232**, 27–32.
- 18 Q. Zhang, L. Pastor-Pérez, W. Jin, S. Gu and T. R. Reina, *Appl. Catal., B*, 2019, **244**, 889–898.
- 19 S.-W. Park, O.-S. Joo, K.-D. Jung, H. Kim and S.-H. Han, *Appl. Catal., A*, 2001, **211**, 81–90.
- 20 X. Su, X. L. Yang, B. Zhao and Y. Q. Huang, *J. Energy Chem.*, 2017, **26**, 854–867.
- 21 Y. A. Daza and J. N. Kuhn, *RSC Adv.*, 2016, **6**, 49675–49691.
- 22 B. Lu and K. Kawamoto, *J. Environ. Chem. Eng.*, 2013, **1**, 300–309.

- 23 P. Quaino, F. Juarez, E. Santos and W. Schmickler, *Beilstein J. Nanotechnol.*, 2014, **5**, 846–854.
- 24 G. Kresse and J. Hafner, *Phys. Rev. B: Condens. Matter Mater. Phys.*, 1993, **47**, 558–561.
- 25 G. Kresse and J. Hafner, *Phys. Rev. B: Condens. Matter Mater. Phys.*, 1994, **49**, 14251–14269.
- 26 G. Kresse and J. Furthmüller, *Comput. Mater. Sci.*, 1996, **6**, 15–50.
- 27 G. Kresse and J. Furthmüller, *Phys. Rev. B: Condens. Matter Mater. Phys.*, 1996, **54**, 11169–11186.
- 28 K. Momma and F. Izumi, *J. Appl. Crystallogr.*, 2011, **44**, 1272–1276.
- 29 J. P. Perdew, K. Burke and M. Ernzerhof, *Phys. Rev. Lett.*, 1996, **77**, 3865–3868.
- 30 P. E. Blöchl, *Phys. Rev. B: Condens. Matter Mater. Phys.*, 1994, **50**, 17953–17979.
- 31 G. Kresse and D. Joubert, *Phys. Rev. B: Condens. Matter Mater. Phys.*, 1999, **59**, 1758–1775.
- 32 S. L. Dudarev, G. A. Botton, S. Y. Savrasov, C. J. Humphreys and A. P. Sutton, *Phys. Rev. B: Condens. Matter Mater. Phys.*, 1998, **57**, 1505–1509.
- 33 U. D. Wdowik and D. Legut, *J. Phys.: Condens. Matter*, 2009, **21**, 275402.
- 34 S. Grimme, J. Antony, S. Ehrlich and H. Krieg, *J. Chem. Phys.*, 2010, **132**, 154104.
- 35 S. Grimme, S. Ehrlich and L. Goerigk, *J. Comput. Chem.*, 2011, **32**, 1456–1465.
- 36 S. Sasaki, K. Fujino and Y. Takéuchi, *Proc. Jpn. Acad., Ser. B*, 1979, **55**, 43–48.
- 37 H. J. Monkhorst and J. D. Pack, *Phys. Rev. B: Solid State*, 1976, **13**, 5188–5192.
- 38 A. Patterson, *Phys. Rev.*, 1939, **56**, 978.
- 39 Y. Zhou, T. Chen, J. Zhang, Y. Liu and P. Ren, *Chin. J. Chem.*, 2017, **35**, 1294–1298.
- 40 G. Zhu, H. Li, L. Deng and Z.-H. Liu, *Mater. Lett.*, 2010, **64**, 1763–1765.
- 41 Z. Khan, S. Park, S. M. Hwang, J. Yang, Y. Lee, H.-K. Song, Y. Kim and H. Ko, *NPG Asia Mater.*, 2016, **8**, e294.
- 42 C.-H. Kim, Z. Akase, L. Zhang, A. H. Heuer, A. E. Newman and P. J. Hughes, *J. Solid State Chem.*, 2006, **179**, 753–774.
- 43 X. Huang, D. Lv, H. Yue, A. Attia and Y. Yang, *Nanotechnology*, 2008, **19**, 225606.
- 44 C. Ji, H. Ren and S. Yang, *RSC Adv.*, 2015, **5**, 21978–21987.
- 45 M. C. Biesinger, B. P. Payne, A. P. Grosvenor, L. W. Lau, A. R. Gerson and R. S. C. Smart, *Appl. Surf. Sci.*, 2011, **257**, 2717–2730.
- 46 R. Pitchai, D. H. Park and G. Campet, *J. Phys. Chem. C*, 2008, **112**, 6588–6588.
- 47 C. Julien, M. Massot, R. Baddour-Hadjean, S. Franger, S. Bach and J. P. Pereira-Ramos, *Solid State Ionics*, 2003, **159**, 345–356.
- 48 E. Cockayne and L. Li, *Chem. Phys. Lett.*, 2012, **544**, 53–58.
- 49 J. Wang, J. Li, P. Zhang and G. Zhang, *Appl. Catal., B*, 2018, **224**, 863–870.
- 50 E. Stobbe, B. De Boer and J. Geus, *Catal. Today*, 1999, **47**, 161–167.
- 51 M. De Falco, S. Giansante, G. Iaquaniello and L. Barbato, in *CO₂: A Valuable Source of Carbon*, Springer, 2013, pp. 171–186.
- 52 L. Pastor-Pérez, F. Baibars, E. Le Sache, H. Arellano-Garcia, S. Gu and T. Reina, *J. CO₂ Util.*, 2017, **21**, 423–428.
- 53 H.-Y. T. Chen, S. Tosoni and G. Pacchioni, *Surf. Sci.*, 2016, **652**, 163–171.
- 54 D. Cornu, H. Guesmi, J.-M. Krafft and H. Lauron-Pernot, *J. Phys. Chem. C*, 2012, **116**, 6645–6654.
- 55 W. Wang, L. Fan, G. Wang and Y. Li, *Appl. Surf. Sci.*, 2017, **425**, 972–977.
- 56 A. K. Mishra, A. Roldan and N. H. de Leeuw, *J. Phys. Chem. C*, 2016, **120**, 2198–2214.
- 57 Y. Zhai, D. Pierre, R. Si, W. Deng, P. Ferrin, A. U. Nilekar, G. Peng, J. A. Herron, D. C. Bell, H. Saltsburg, M. Mavrikakis and M. Flytzani-Stephanopoulos, *Science*, 2010, **329**, 1633–1636.
- 58 X. Yang, X. Su, X. Chen, H. Duan, B. Liang, Q. Liu, X. Liu, Y. Ren, Y. Huang and T. Zhang, *Appl. Catal., B*, 2017, **216**, 95–105.
- 59 G. Rothenberg, *Catalysis: concepts and green applications*, John Wiley & Sons, 2017.
- 60 T. Bligaard, J. K. Nørskov, S. Dahl, J. Matthiesen, C. H. Christensen and J. Sehested, *J. Catal.*, 2004, **224**, 206–217.